



CHORUS

This is the accepted manuscript made available via CHORUS. The article has been published as:

Site-resolved imaging of single atoms with a Faraday quantum gas microscope

Ryuta Yamamoto, Jun Kobayashi, Kohei Kato, Takuma Kuno, Yuto Sakura, and Yoshiro Takahashi

Phys. Rev. A **96**, 033610 — Published 8 September 2017

DOI: [10.1103/PhysRevA.96.033610](https://doi.org/10.1103/PhysRevA.96.033610)

Site-resolved imaging of single atoms with a Faraday quantum gas microscope

Ryuta Yamamoto,* Jun Kobayashi, Kohei Kato,† Takuma Kuno, Yuto Sakura, and Yoshiro Takahashi
Department of Physics, Graduate School of Science, Kyoto University, Kyoto 606-8502, Japan

(Dated: August 11, 2017)

We demonstrate a quantum gas microscope based on the Faraday effect that does not require a stochastic spontaneous emission process. We reveal the dispersive feature of this Faraday-imaging method by comparing the detuning dependence of the Faraday signal with that of the photon scattering rate. In addition, we determine the atom distribution through a deconvolution analysis, demonstrate absorption and dark-field Faraday imaging, and reveal the various shapes of the point spread functions for these methods, which are fully explained by a theoretical analysis. The results constitute an important first step toward ultimate quantum nondemolition site-resolved imaging and open the way to quantum feedback control of a quantum many-body system with single-site resolution.

PACS numbers: 67.85.Hj, 07.60.Pb, 37.10.Jk, 78.20.Ls

At the heart of quantum information processing lies the measurement and manipulation of each quantum object in a quantum many-body system [1]. For ultracold atoms in an optical lattice, the technique of single-site-resolved imaging and single-site-addressing, called “quantum gas microscopy” (QGM), has been recently demonstrated for bosons [2–5] and fermions [6–10]. The development of the QGM technique enables us to realize various fascinating experiments to study quantum many-body systems [11–16], which are almost impossible to perform with other techniques. Current QGM methods, however, detect atoms by detecting photons spontaneously emitted from atoms. This process is inherently stochastic, so the many-body state is inevitably projected onto a product state of single atoms. In addition, the measurement induces considerable recoil heating, requiring an elaborate cooling scheme in a deep optical lattice.

Advanced methods to implement quantum nondemolition (QND) measurements and quantum feedback control have been demonstrated for several systems, such as a cavity quantum electrodynamics (QED) system [18, 19], a collective spin ensemble [20–26], and a circuit QED system [27]. To realize quantum measurement and control of each atom in an optical lattice, a new detection method for QGM is required that does not rely on a destructive fluorescence measurement. Promising results along these lines have already been reported in the form of detection of single atoms trapped by a tightly focused laser beam and those trapped in an ion trap via dispersive methods (see Refs. [28] and [29], respectively). Here we note that, although the use of an optical cavity provides an intriguing sensitivity for a single atom [30–32], this cannot simply be combined with a QGM technique because the

cavity spatial mode determines the spatial resolution, so single-site resolution is not expected.

In this paper, we present a detection method for QGM based on the dispersive Faraday effect (Faraday QGM) to achieve site-resolved imaging of single isolated atoms in an optical lattice. The observed Faraday rotation angle reaches $3.0(2)^\circ$ for a single atom. Contrary to current QGM methods, Faraday imaging allows us to measure the density distribution of a quantum many-body state without projecting onto a product state over each site, which allows us to make continuous observations of multiparticle quantum dynamics [33]. An interesting example that uses a QND-type measurement is the study of quantum critical behavior of Bose-Hubbard systems influenced by measurement backaction [34]. From a technical viewpoint, the realization of the minimally destructive limit of Faraday QGM should significantly relax the crucial requirement of incorporating an elaborate cooling scheme for an extremely deep optical lattice depth for QGM based on fluorescence detection. This feature can extend QGM to various atomic species and even to molecules. Furthermore, the Faraday-imaging technique inherently enables us to measure, in principle, an arbitrary number of atoms per site without relying on a sophisticated bilayer or superlattice configuration to circumvent parity projection [9, 35]. Note that the results reported herein do not correspond to a QND regime because the atoms experience absorption in the current experimental conditions.

In our experiment, we use bosonic ytterbium (^{174}Yb) atoms. First, we prepare a Bose-Einstein condensate (BEC) of ^{174}Yb atoms in an optical trap, and then load it into a single layer of a two-dimensional (2D) optical lattice with lattice spacing of 266 nm. In a previous study, by site-resolved fluorescence imaging, we observed single isolated atoms with a dual molasses technique [5]. In the present study, we detect the polarization rotation of a linearly polarized probe transmitted through atoms in a 2D optical lattice, as shown schematically in Fig. 1(a).

The polarization rotation signal due to the Faraday

* Electronic address: r_yamamoto@scphys.kyoto-u.ac.jp; Present address: RIKEN Center for Emergent Matter Science, Hiroswa, Wako, Saitama 351-0198, Japan

† Present address: Department of Physics, Osaka City University, Sumiyoshi-ku, Osaka 558-8585, Japan

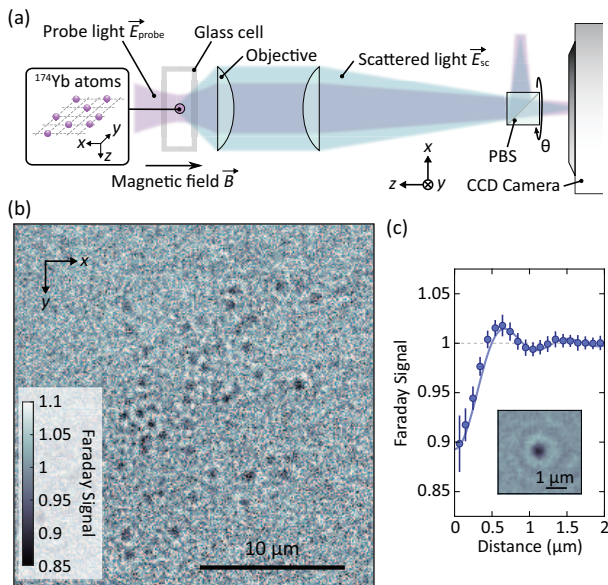


FIG. 1. Faraday imaging. (a) Schematic of the imaging system. We detect the polarization rotation of a 399 nm linearly polarized probe beam transmitted through ^{174}Yb atoms in a 2D optical lattice. A polarizing beam splitter (PBS) is situated in front of the CCD camera. A high-resolution objective with the numerical aperture $\text{NA} = 0.75$ is fixed just above the glass cell. The PBS angle θ is set to be $\pi/4$ for Faraday imaging. (b) Site-resolved Faraday image of ^{174}Yb atoms. The probe beam is detuned by $2\delta_B/\Gamma \sim 3.9$ and the intensity is 1.3×10^{-2} times the saturation intensity, which corresponds to a saturation parameter [17] of 0.84×10^{-3} . The measurement duration is 400 ms. (c) Measured point spread function (PSF) averaged over about 30 individual single atoms and azimuthal average of the PSF. The blue line is a fit to Eq. (2) with $\text{NA} = 0.49(2)$.

effect for a single atom can be understood as an effect of interference between a linearly polarized input probe beam $\vec{E}_{\text{probe}}(r)$ and an electric field scattered by a single atom. Based on diffraction theory [36] and scattering theory [37], the scattered light field $\vec{E}_{\text{sc}}(r)$ is described as

$$\vec{E}_{\text{sc}}(r) = \alpha \frac{2J_1(r/\sigma)}{r/\sigma} E_0 \left(\frac{\hat{e}_+}{1 - i(2\delta_B/\Gamma)} + \frac{\hat{e}_-}{1 + i(2\delta_B/\Gamma)} \right), \quad (1)$$

where δ_B represents the detuning from resonance. For all measurements reported herein, we set the frequency of the probe beam at the center of 1S_0 - 1P_1 ($m_J = \pm 1$) transitions, unless otherwise noted (see Fig. 5 for the relevant energy diagram). Thus, the probe beam is detuned equally with respect to 1S_0 - 1P_1 ($m_J = \pm 1$) transitions and is polarized perpendicular to the quantization axis, and the detuning is provided by an applied magnetic field (see Appendix A for details). E_0 is the amplitude of the electric field of the input probe beam, $\alpha = -(3\eta)^{1/2} \text{NA}/2$, where NA is the numerical aperture of the objective, $\eta \equiv [1 - (1 - \text{NA}^2)^{1/2} (1 - \text{NA}^2/4)]/2$ is

the photon collection efficiency of the objective, $J_1(x)$ is the Bessel function of the first kind, $\sigma \equiv (k\text{NA})^{-1}$ is the diffraction-limited spatial resolution, k is the wavenumber of probe light, and \hat{e}_{\pm} is the polarization unit vector for σ_{\pm} circularly polarized light. By using these expressions, the total detected electric field $E_{\text{detect}}(r)$ after polarizing beam splitter (PBS) is $E_{\text{detect}}(r) = (\vec{E}_{\text{probe}}(r) + \vec{E}_{\text{sc}}(r)) \cdot \hat{e}_{\theta}$, where θ and \hat{e}_{θ} represent the angle of PBS with respect to incident probe polarization and its unit vector, respectively. In our experimental setup, the beam waist of the probe beam is $\sim 37 \mu\text{m}$, which is much larger than the experimentally measured resolution σ_{exp} of about 120 nm [38], so the probe beam may be considered to be spatially uniform. The Faraday image of a single atom, with the background level normalized to unity, can be described as

$$I_{\text{detect}}(r) = |E_{\text{detect}}(r)/(E_0 \cos \theta)|^2 = \left| 1 + \sqrt{2}\alpha \frac{1 + (2\delta_B/\Gamma) \tan \theta}{1 + (2\delta_B/\Gamma)^2} \frac{2J_1(r/\sigma)}{r/\sigma} \right|^2 \quad (2)$$

Note that this spatial profile of the image of a single atom, namely the point spread function (PSF), differs from that of fluorescence imaging. A fluorescence image records the scattered light intensity proportional to $(2J_1(x)/x)^2$. For a Faraday image at a PBS angle $\theta = \pm\pi/4$, however, the interference term between the probe light $\vec{E}_{\text{probe}}(r)$ and the scattered light $\vec{E}_{\text{sc}}(r)$, which is proportional to $2J_1(x)/x$, becomes dominant. This PSF, which differs from that of a fluorescence image, appears in Fig. 1(c) and is discussed below.

Note also that our Faraday image is equivalent to phase-contrast polarization imaging developed in Ref. [39] and can be used for nondestructive probing of a BEC. However, compared to the nondestructive imaging of a BEC in which the state is protected by the large number of atoms in the condensate, the requirement for nondestructive imaging is much more stringent and demands for single-atom detection by QGM.

Figure 1(b) shows an example of a Faraday image obtained with the measurement setup shown in Fig. 1(a) and with a PBS angle $\theta = \pi/4$. To more easily evaluate the performance of Faraday QGM, we prepare a sparse cloud of atoms with very low lattice filling. For this purpose, we transfer a small fraction of atoms from the ground state 1S_0 to the metastable state 3P_2 by irradiation with a low-intensity laser, following which the remaining atoms in the 1S_0 state are removed by applying the resonance light of 1S_0 - 1P_1 transition. Finally, the atoms are de-excited from the 3P_2 state to the 1S_0 state by repumping [5]. The observed Faraday rotation angle reaches $3.0(2)^\circ$ for a single atom with the detuning $2\delta_B/\Gamma \sim 3.9$ (see Appendix C for details). Figure 1(c) shows the measured PSF, which is obtained by averaging over about 30 individual isolated atoms. The measured PSF is well fit by using Eq. (2), as shown by the blue solid line in Fig. 1(c).

We determine the atom distribution by deconvolution

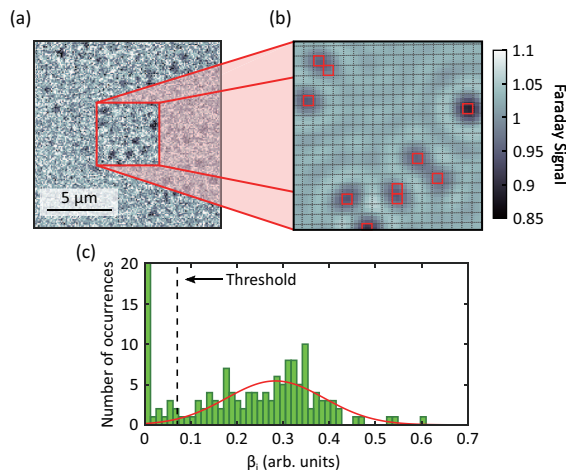


FIG. 2. Deconvolution result of Faraday QGM. (a) Raw Faraday image of lattice sparsely filled with atoms. (b) Numerically reconstructed distribution of atoms on lattice sites. The image is the convolution of the model PSF of Eq. (2) and the reconstructed atom distribution. Red squares and gray dotted lines represent the atoms and the lattice cells, respectively. (c) Histogram of the fitting parameters β_i in each site. A black dashed line shows the threshold for the presence of atoms. The red solid curve is a fit to the data with a Gaussian function. We set the threshold value at 2σ below the center of the Gaussian.

of the Faraday images. The basic deconvolution procedure is almost the same as that used in our previous work on fluorescence imaging by QGM [5]. For the deconvolution of Faraday images, we calculate the estimated image intensity at position \vec{r} by using

$$I_{\text{est}}(\vec{r}) = \left| 1 + \Delta_{\text{BG}} + \sum_i^{N_{\text{site}}} \beta_i \frac{\vec{E}_{\text{sc}}(|\vec{r} - \vec{r}_i|) \cdot \hat{e}_\theta}{E_0 \cos \theta} \right|^2, \quad (3)$$

where Δ_{BG} is the difference from unity of the background level of the Faraday image, and \vec{r}_i and β_i are the center position and amplitude, respectively, of the signal per lattice site i . Figure 2(a) shows a raw image from Faraday QGM, and Fig. 2(b) shows the reconstructed atom distribution convoluted with the model PSF. Figure 2(c) shows a histogram of the fitting parameters β_i for each site, where the black dashed line indicates the threshold for the presence of atoms.

The Faraday signal, which is the interference term in Eq. (2), is inversely proportional to the detuning ($\propto 1/\delta_B$) in the limit of large detuning. Because the destructive effect of photon scattering is controlled by the photon scattering rate Γ_{sc} , we compare the Faraday signal to Γ_{sc} , which is proportional to $1/\delta_B^2$ in the limit of large detuning. By using a large detuning, we improve the ratio of the signal strength to the destructive effect of photon scattering in Faraday imaging. Figure 3 shows how the ratio of Faraday-imaging signal strength S_{FI} to the fluorescence-imaging signal strength S_{FL} depends on detuning (in arbitrary units). Note that the Faraday-

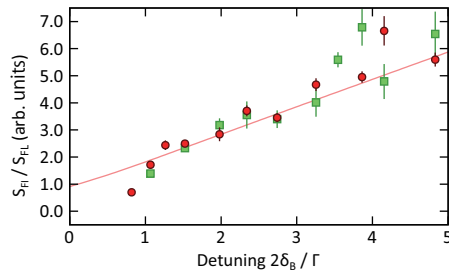


FIG. 3. Ratio of signal strength of Faraday imaging S_{FI} to that of fluorescence imaging S_{FL} , which is proportional to the photon scattering rate Γ_{sc} for Faraday imaging. The green squares represent the data obtained from signals from isolated atoms, and the red circles represent the ensemble measurements. The solid curve is a fit based on the weak-excitation approximation, which is plausible in the given experimental conditions but not in case of far off resonance. Note that we use the value of α for the effective NA of 0.49(2) in our setup.

imaging signal strength S_{FI} is given by the average signal of the isolated atoms in Faraday imaging and we use $S_{\text{FI}} \equiv \int d\vec{r} [1 - I_{\text{detect}}(r)]$. The averaged signal from isolated atoms in fluorescence imaging acquired at the same detuning S_{FL} is used to measure the photon scattering rate Γ_{sc} . The ratios obtained in this way are denoted by green squares. We also plot the ratios obtained by ensemble measurements as red circles. The experimental results are consistent with the theoretical prediction shown by the solid lines, and in particular, increase linearly with the detuning, which indicates that Faraday imaging allows single-atom detection with reduced spontaneous photon scattering. In fact, the saturation parameter at the detuning $2\delta_B/\Gamma \sim 4.8$ corresponds to 0.6×10^{-3} , which is almost half of the value for a typical fluorescence image. This is to be contrasted with the case of fluorescence imaging where the ratio is constant and does not improve with detuning.

We now discuss the current limitation of Faraday imaging and possible remedies. The Faraday signal comes from the interference between scattered light and probe light. Thus, the background level of the Faraday signal is sensitive to the temporal fluctuation and the spatial inhomogeneity of the probe beam intensity and polarization, resulting in a relatively poor signal-to-noise ratio (SNR). This problem can, in principle, be solved by careful stabilization of the probe beam in terms of intensity, polarization, and spatial profile. Note that the extinction ratio of the polarization analyzer is not crucial in the Faraday-imaging method proposed herein with a PBS angle $\theta = \pm\pi/4$. In the present experiment, the SNR is further limited by the finite spatial resolution. Therefore, we use a high-intensity probe light to obtain a better SNR. This causes absorption and spontaneous emission, which heats the atoms. To maintain the atoms in the same lattice sites, we irradiate the sample with cooling light during imaging. In contrast, if we consider the ideal conditions where $\text{NA} = 1$ and intensity and polarization

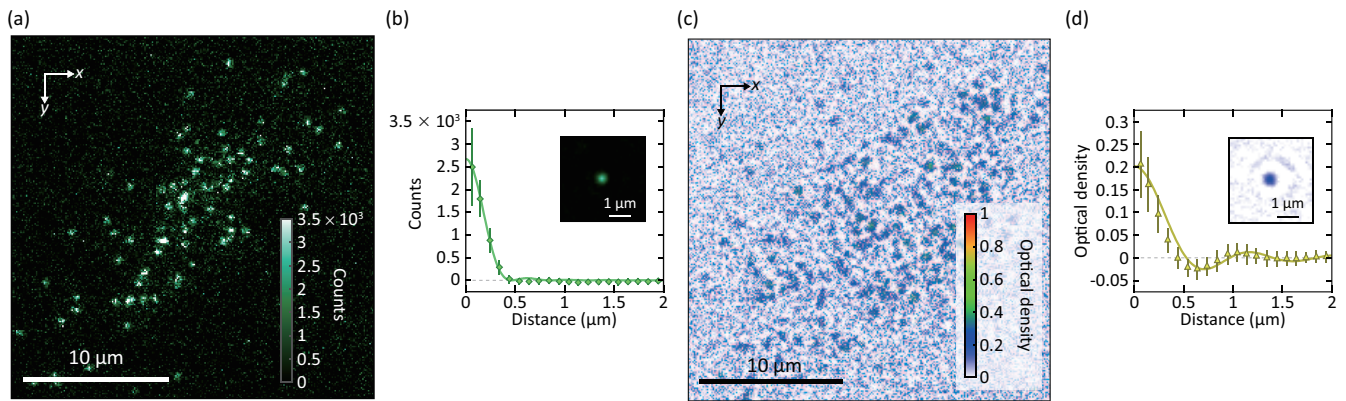


FIG. 4. Site-resolved DFFI and absorption imaging. (a) DFFI ($\theta = \pi/2$). Probe beam detuning is $2\delta_B/\Gamma \sim 3.9$ and the intensity is 1.7×10^{-2} times the saturation intensity, which corresponds to a saturation parameter of 1.1×10^{-3} . (b) Measured PSF averaged over about 30 individual atoms and azimuthal average of DFFI. The green solid line is a fit to Eq. (4). (c) Absorption imaging ($\theta = 0$). The detuning of the probe beam is $2\delta_B/\Gamma \sim 0.76$ and the intensity is 4.7×10^{-3} times the saturation intensity, which corresponds to a saturation parameter of 2.9×10^{-3} . (d) Measured PSF averaged over about 60 individual atoms and azimuthal average of absorption image. The yellow solid line is a fit to $-\ln[I_{\text{detect}}(r)]$, where $I_{\text{detect}}(r)$ is given by Eq. (2). The duration of each measurement is 400 ms.

fluctuations are absent, only shot-noise remains. However, we still estimate an $\text{SNR} \sim 1$ for a small number of the spontaneous photon-scattering events during the measurement, consistent with the previous arguments in different situations [40, 41]. An $\text{SNR} \sim 1$ would limit the applicability of the method, especially for imaging a dense cloud.

To increase the SNR, we must tolerate a larger number of photon-scattering events and the resulting heating effect. However, we estimate that this heating effect, although present, may be kept small enough so that atoms do not escape the lattice. This approach relaxes the cooling requirement and the optical lattice depth during imaging, as mentioned above. As experimentally realistic parameters, we use a detuning $2\delta_B/\Gamma = 30$ and $N_0 = 1200$ detected photons from the probe beam, for which shot-noise-limited performance is expected with the current level of polarization stability. Although technically challenging, it is also possible to increase the SNR by using the polarization-squeezed state [42, 43], as has been recently demonstrated in high-sensitivity spectroscopy of a thermal gas [44]. In the present study, the detuning $2\delta_B/\Gamma$ is limited by the amplitude of the applied magnetic field. The use of $^1S_0 \rightarrow ^3P_1$ transition, which has much smaller Γ , is an interesting possibility for a future demonstration of Faraday imaging at the large detuning $2\delta_B/\Gamma$.

In addition to Faraday imaging with the PBS angle $\theta = \pi/4$, we demonstrate a different type of Faraday imaging, namely dark-field Faraday imaging (DFFI) [45], for which $\theta = \pi/2$ in the setup of Fig. 1(a). In this case, PBS reflects 100% of the probe light and only the scattered light is transmitted by PBS and detected by the CCD camera. This configuration for DFFI allows us to obtain a background-free signal similar to a fluorescence signal. Again, we prepare a sparse cloud of atoms in the

same way as for the Faraday imaging shown in Fig. 1(b). Figure 4(a) shows the DFFI signal of a site-resolved image of single atoms. Here, the detuning is $2\delta_B/\Gamma \sim 3.9$, which is the same as that in Fig. 1(b) for Faraday imaging. Although this DFFI signal appears quite similar to that of fluorescence imaging, it originates from a dispersive interaction, just like the Faraday signal. Figure 4(b) shows the measured PSF, which is obtained by averaging over about 30 individual atoms. The measured PSF is well fit by

$$I_{\text{DFFI}}(r) \propto \left(\frac{2\delta_B/\Gamma}{1 + (2\delta_B/\Gamma)^2} \frac{2J_1(r/\sigma)}{r/\sigma} \right)^2, \quad (4)$$

and the green solid line in Fig. 4(b) shows the fit with Eq. (4). Note that, in the limit of large detuning, the DFFI signal has a detuning dependence of $\propto 1/\delta_B^2$ and is not a nondestructive measurement. The experimental results show the saturation of the ratio of the DFFI signal to the photon-scattering rate Γ_{sc} at larger detuning, consistent with theory and indicating that DFFI has no merit for realizing single-atom detection with reduced spontaneous photon scattering.

In addition, we demonstrate absorption imaging by using the PBS angle $\theta = 0$, which is the standard setup for an ensemble measurement. In this case, similar to Faraday imaging, the probe light interferes destructively (and also constructively) with the scattered light. Figure 4(c) shows the absorption image, which clearly constitutes a site-resolved image of single atoms. Here, the detuning is $2\delta_B/\Gamma \sim 0.76$, which is within the linewidth of the probe transition. Figure 4(d) shows the measured PSF, which is obtained by averaging over about 60 individual atoms and which reveals the interference features similar to the case of Faraday imaging. Again, we find that our measured PSF is well fit by $-\ln[I_{\text{detect}}(r)]$, as shown by the

yellow solid line in Fig. 4(d), and the peak optical density of PSF reaches 0.20(2), which corresponds to a maximum extinction of 18(1)% by a single atom. This value is much greater than that obtained in previous single-atom or -ion experiments [46, 47].

In conclusion, we use the Faraday effect to demonstrate site-resolved imaging of single atoms. The observed Faraday rotation angle reaches $3.0(2)^\circ$ for a single atom. We demonstrate the nondestructive nature of this Faraday-imaging method by investigating the detuning dependence of the signal. In addition, we demonstrate absorption imaging and DFFI by QGM and reveal the different shapes of PSFs for these imaging methods, which are fully explained by theory. These results constitute an important step toward a QND measurement with single-site resolution. Furthermore, they should open way for quantum feedback control of individual atoms in quantum many-body systems, which should have significant impact on quantum information processing and the physics of quantum many-body systems.

The authors are grateful to E. Chae, S. Yamanaka, and Y. Amano for careful reading of the manuscript. This work was supported by the Grant-in-Aid for Scientific Research of JSPS (Nos. 13J00122, 25220711, 26247064, 26610121, 16H00990, and 16H01053) and the Impulsing Paradigm Change through Disruptive Technologies (IMPACT) program.

Appendix A: Low-lying energy levels of ytterbium atom

Figure 5 shows the low-lying energy levels associated with probing. We apply a magnetic field \vec{B} to induce the Faraday effect; \vec{B} is almost parallel to the z -axis, which is the propagation direction of a probe beam, as shown in Fig. 1(a). A linearly polarized probe beam is near resonant with the 1S_0 - $^1P_1(m_J = \pm 1)$ transition (transition wavelength $\lambda = 399$ nm and natural

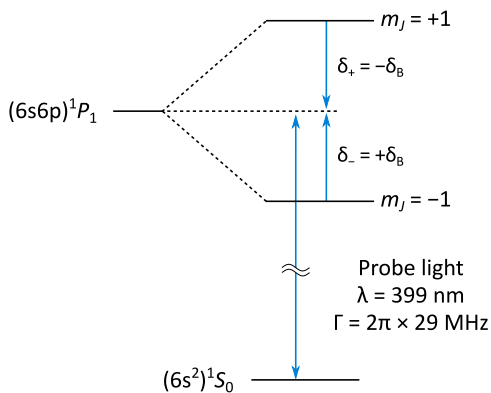


FIG. 5. Low-lying energy levels of ^{174}Yb atom relevant for probing. The frequency of the probe beam is set at the center of 1S_0 - $^1P_1(m_J = 1)$ and 1S_0 - $^1P_1(m_J = -1)$ transitions.

linewidth $\Gamma = 2\pi \times 29$ MHz). Unless otherwise noted, the measurements in this study were performed with the frequency of the probe beam at the center of the 1S_0 - $^1P_1(m_J = \pm 1)$ transitions. Thus, the detuning of the probe beam with respect to 1S_0 - $^1P_1(m_J = \pm 1)$ transition is $\mp\delta_B$. Here, $\delta_B = g_J\mu_B|\vec{B}|/\hbar$ is the Zeeman shift in the $^1P_1(m_J = \pm 1)$ state due to the magnetic field \vec{B} , g_J is the Landé g -factor of the 1P_1 state, and μ_B is the Bohr magneton (Fig. 5). Because the applied magnetic field is almost parallel to the z -axis, we have negligible excitation in 1S_0 - $^1P_1(m_J = 0)$ transition.

Appendix B: Optical Spectra of Faraday imaging, DFFI, and absorption imaging

Figure 6 shows the optical spectra for (a) Faraday imaging, (b) DFFI, and (c) absorption imaging, where the total counts in each panel is plotted as a function of the detuning of probe beam δ_0 . Here, a magnetic field of 40 G is applied for Faraday imaging and DFFI, and 8 G for absorption imaging. The resonance positions are indicated by arrows in the figure.

The Faraday imaging shows a dispersive frequency dependence around 1S_0 - $^1P_1(m_J = \pm 1)$ resonances

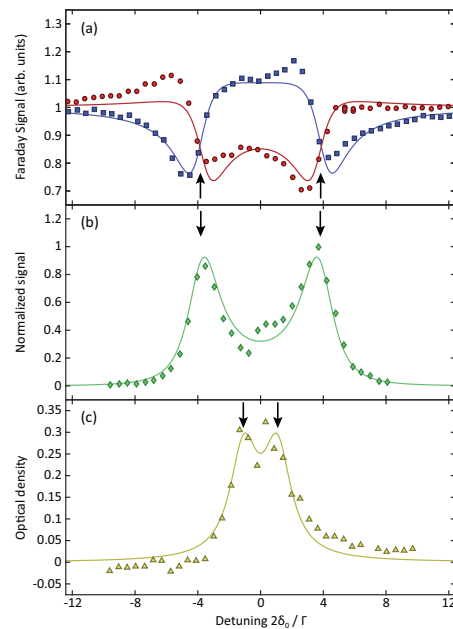


FIG. 6. Optical spectra of (a) Faraday imaging ($\theta = \pm\pi/4$), (b) DFFI ($\theta = \pi/2$), and (c) absorption imaging ($\theta = 0$). A magnetic field of 40 G is applied for Faraday imaging and DFFI, and 8 G for absorption imaging. The resonance positions are indicated by arrows in each panel. (a) The red (blue) curve shows the spectrum with a PBS angle $\theta = \pi/4$ ($-\pi/4$). (b) The solid line shows the fit with Eq. (B3). The signal strength in each spectrum is proportional to the total counts for the given image.

($2\delta_0/\Gamma \sim \pm 3.9$), which can be fit with

$$A_{\text{FI}}(\delta_0) = \left| \frac{(\vec{E}_{\text{probe}} + \vec{E}_{\text{sc}}(\delta_0)) \cdot \hat{e}_\theta}{\vec{E}_{\text{probe}} \cdot \hat{e}_\theta} \right|^2, \quad (\text{B1})$$

where

$$\vec{E}_{\text{sc}}(\delta_0) \propto \left(\frac{\hat{e}_+}{1 + i2(\delta_0 - \delta_B)/\Gamma} + \frac{\hat{e}_-}{1 + i2(\delta_0 + \delta_B)/\Gamma} \right). \quad (\text{B2})$$

In Fig. 6(a), the red (blue) curve shows the fit with $\theta = \pi/4$ ($\theta = -\pi/4$).

The DFFI signal can be described by

$$\begin{aligned} A_{\text{DFFI}}(\delta_0) &\propto \left| \vec{E}_{\text{sc}}(\delta_0) \cdot \hat{e}_{\pi/2} \right|^2 \\ &\propto \left| \frac{1}{1 + i2(\delta_0 - \delta_B)/\Gamma} - \frac{1}{1 + i2(\delta_0 + \delta_B)/\Gamma} \right|^2. \end{aligned} \quad (\text{B3})$$

The solid line in Fig. 6(b) shows the fit to Eq. (B3).

The absorption image shows a resonance that can be fit to $-\ln[A_{\text{FI}}(\delta_0)]$ with $\theta = 0$, as shown in Fig. 6(c).

Appendix C: Faraday rotation angle of a single atom

The intensity $I_{\text{detect}}(r)$ given in Eq. (2) may also be described as $I_{\text{detect}}(r) = [\cos(\theta + \phi(r))/\cos\theta]^2$ by introducing a position-dependent Faraday rotation angle $\phi(r)$ defined as $\vec{E}_{\text{probe}}(r) + \vec{E}_{\text{sc}}(r) = E_0(e^{+i\phi(r)}\hat{e}_+ + e^{-i\phi(r)}\hat{e}_-)/\sqrt{2}$. Therefore, $\phi(r)$ can be calculated by using

$$\phi(r) = \cos^{-1} \left[(I_{\text{detect}}(r) \cos^2 \theta)^{1/2} \right] - \theta. \quad (\text{C1})$$

From the data shown in Fig. 1(c) and by using Eq. (C1) with $\theta = \pi/4$, we evaluate the spatial distribution of the Faraday rotation angle of a single atom and its azimuthal average. The result appears in Fig. 7.

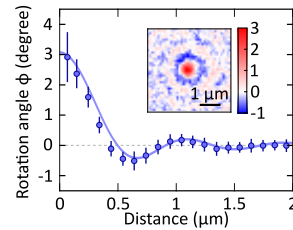


FIG. 7. Azimuthal average of Faraday rotation angle evaluated using Eq. (C1). The detuning of the probe light is $2\delta_B/\Gamma \sim 3.9$ with the saturation parameter $s_{399} = 0.84 \times 10^{-3}$. The peak Faraday rotation angle is $3.0(2)^\circ$.

Appendix D: Effect of a probe beam for Faraday quantum gas microscopy

Usually, image fidelity can be evaluated by taking two successive images of the same atoms and comparing the atom distributions. The fidelity deduced from such a method includes the fidelity of the deconvolution procedure, which makes a large contribution to the current Faraday-imaging technique, especially at low probe intensities. Here, to extract only the effect of the probe light for Faraday imaging, we apply a probe pulse with the same detuning as the Faraday imaging and vary the intensity during the 400 ms interval between the two images. The timing involved in acquiring two consecutive images and applying the probe beam is shown schematically in Fig. 8(a). The two consecutive images to determine the atom distributions are acquired with the PBS angle set to $\pi/2$ (DFFI) to obtain a background-free image similar to that of fluorescence images. Note that the cooling light is also applied to suppress the residual heating effect, as done for Faraday imaging. Figure 8(b) shows the fidelity normalized by the image with no probe light during two image cycles. Almost no change appears in the pinned, loss, and hopping fractions when the probe intensity is less than 2×10^{-2} times the saturation intensity. Note that most of the measurements in this paper were performed in this regime. Above this intensity, the loss and hopping fractions increase almost linearly. This behavior is reasonable when considered in terms of the saturation parameter. The observed critical value corresponds to a saturation parameter of $s_{399} \sim 10^{-3}$, which is consistent with that observed in the previous experiment, where the heating effect of the probe beam was balanced by cooling.

-
- [1] M. A. Nielsen and I. L. Chuang, *Quantum computation and quantum information* (Cambridge university press, 2010).
- [2] W. S. Bakr, J. I. Gillen, A. Peng, S. Fölling, and M. Greiner, *Nature* **462**, 74 (2009).
- [3] C. Weitenberg, M. Endres, J. F. Sherson, M. Cheneau, P. Schauß, T. Fukuhara, I. Bloch, and S. Kuhr, *Nature* **471**, 319 (2011).

- [4] M. Miranda, R. Inoue, Y. Okuyama, A. Nakamoto, and M. Kozuma, *Phys. Rev. A* **91**, 063414 (2015).
- [5] R. Yamamoto, J. Kobayashi, T. Kuno, K. Kato, and Y. Takahashi, *New J. Phys.* **18**, 023016 (2016).
- [6] L. W. Cheuk, M. A. Nichols, M. Okan, T. Gersdorf, V. V. Ramasesh, W. S. Bakr, T. Lompe, and M. W. Zwierlein, *Phys. Rev. Lett.* **114**, 193001 (2015).
- [7] E. Haller, J. Hudson, A. Kelly, D. A. Cotta, B. Peaudecerf, G. D. Bruce, and S. Kuhr, *Nat. Phys.* **11**, 738

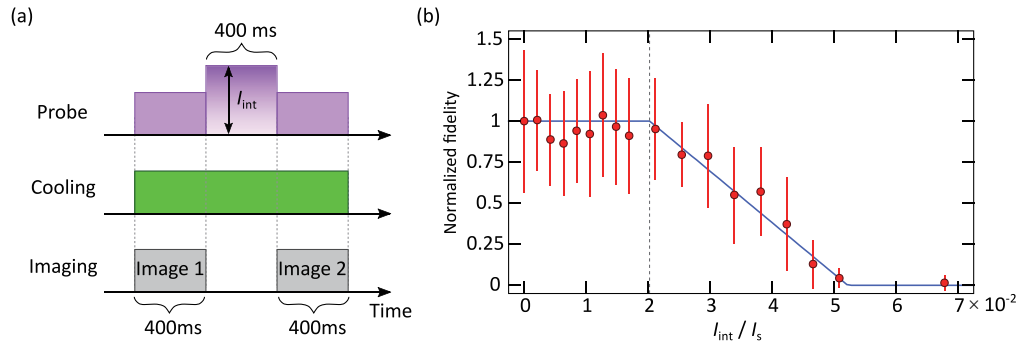


FIG. 8. Effect of probe light for Faraday QGM. (a) Timing for acquiring two consecutive images while varying the probe intensity. The exposure time and interval time are 400 ms. (b) Measured fidelity normalized by the fidelity with no probe light as a function of probe intensity. Below the intensity $I_{\text{int}} = 2 \times 10^{-2} I_s$, the normalized fidelity is almost unity. Note that I_s is the saturation intensity of the probe beam.

- (2015).
- [8] M. F. Parsons, F. Huber, A. Mazurenko, C. S. Chiu, W. Setiawan, K. Wooley-Brown, S. Blatt, and M. Greiner, *Phys. Rev. Lett.* **114**, 213002 (2015).
- [9] A. Omran, M. Boll, T. A. Hilker, K. Kleinlein, G. Salomon, I. Bloch, and C. Gross, *Phys. Rev. Lett.* **115**, 263001 (2015).
- [10] G. J. A. Edge, R. Anderson, D. Jervis, D. C. McKay, R. Day, S. Trotzky, and J. H. Thywissen, *Phys. Rev. A* **92**, 063406 (2015).
- [11] H. Ott, *Rep. Prog. Phys.* **79**, 054401 (2016).
- [12] R. Islam, R. Ma, P. M. Preiss, M. Eric Tai, A. Lukin, M. Rispoli, and M. Greiner, *Nature* **528**, 77 (2015).
- [13] M. F. Parsons, A. Mazurenko, C. S. Chiu, G. Ji, D. Greif, and M. Greiner, *Science* **353**, 1253 (2016).
- [14] M. Boll, T. A. Hilker, G. Salomon, A. Omran, J. Nespolo, L. Pollet, I. Bloch, and C. Gross, *Science* **353**, 1257 (2016).
- [15] J.-y. Choi, S. Hild, J. Zeiher, P. Schauß, A. Rubio-Abadal, T. Yefsah, V. Khemani, D. A. Huse, I. Bloch, and C. Gross, *Science* **352**, 1547 (2016).
- [16] L. W. Cheuk, M. A. Nichols, K. R. Lawrence, M. Okan, H. Zhang, E. Khatami, N. Trivedi, T. Paiva, M. Rigol, and M. W. Zwierlein, *Science* **353**, 1260 (2016).
- [17] C. Cohen-Tannoudji, J. Dupont-Roc, G. Grynberg, and P. Thickstun, *Atom-photon interactions: basic processes and applications* (Wiley Online Library, 1992).
- [18] C. Guerlin, J. Bernu, S. Deleglise, C. Sayrin, S. Gleyzes, S. Kuhr, M. Brune, J.-M. Raimond, and S. Haroche, *Nature* **448**, 889 (2007).
- [19] C. Sayrin, I. Dotsenko, X. Zhou, B. Peaudecerf, T. Rybarczyk, S. Gleyzes, P. Rouchon, M. Mirrahimi, H. Amini, M. Brune, J.-M. Raimond, and S. Haroche, *Nature* **477**, 73 (2011).
- [20] G. A. Smith, S. Chaudhury, A. Silberfarb, I. H. Deutsch, and P. S. Jessen, *Phys. Rev. Lett.* **93**, 163602 (2004).
- [21] J. Appel, P. J. Windpassinger, D. Oblak, U. B. Hoff, N. Kjærgaard, and E. S. Polzik, *Proc. Natl. Acad. Sci. U.S.A.* **106**, 10960 (2009).
- [22] T. Takano, M. Fuyama, R. Namiki, and Y. Takahashi, *Phys. Rev. Lett.* **102**, 033601 (2009).
- [23] M. H. Schleier-Smith, I. D. Leroux, and V. Vuletić, *Phys. Rev. Lett.* **104**, 073604 (2010).
- [24] R. J. Sewell, M. Koschorreck, M. Napolitano, B. Dubost, N. Behbood, and M. W. Mitchell, *Phys. Rev. Lett.* **109**, 253605 (2012).
- [25] R. Inoue, S.-I.-R. Tanaka, R. Namiki, T. Sagawa, and Y. Takahashi, *Phys. Rev. Lett.* **110**, 163602 (2013).
- [26] K. C. Cox, G. P. Greve, J. M. Weiner, and J. K. Thompson, *Phys. Rev. Lett.* **116**, 093602 (2016).
- [27] K. W. Murch, S. J. Weber, C. Macklin, and I. Siddiqi, *Nature* **502**, 211 (2013).
- [28] S. A. Aljunid, M. K. Tey, B. Chng, T. Liew, G. Maslennikov, V. Scarani, and C. Kurtsiefer, *Phys. Rev. Lett.* **103**, 153601 (2009).
- [29] A. Jechow, B. G. Norton, S. Händel, V. Blüms, E. W. Streed, and D. Kielpinski, *Phys. Rev. Lett.* **110**, 113605 (2013).
- [30] C. J. Hood, M. S. Chapman, T. W. Lynn, and H. J. Kimble, *Phys. Rev. Lett.* **80**, 4157 (1998).
- [31] P. Maunz, T. Puppe, I. Schuster, N. Syassen, P. W. H. Pinkse, and G. Rempe, *Nature* **428**, 50 (2004).
- [32] J. D. Thompson, T. G. Tiecke, N. P. de Leon, J. Feist, A. V. Akimov, M. Gullans, A. S. Zibrov, V. Vuletić, and M. D. Lukin, *Science* **340**, 1202 (2013).
- [33] Y. Ashida and M. Ueda, *Phys. Rev. A* **95**, 022124 (2017).
- [34] Y. Ashida, S. Furukawa, and M. Ueda, *Phys. Rev. A* **94**, 053615 (2016).
- [35] P. M. Preiss, R. Ma, M. E. Tai, J. Simon, and M. Greiner, *Phys. Rev. A* **91**, 041602 (2015).
- [36] L. Novotny and B. Hecht, *Principles of nano-optics* (Cambridge university press, 2012).
- [37] M. K. Tey, G. Maslennikov, T. C. H. Liew, S. A. Aljunid, F. Huber, B. Chng, Z. Chen, V. Scarani, and C. Kurtsiefer, *New J. Phys.* **11**, 043011 (2009).
- [38] Note that the theoretically predicted resolution σ_{ideal} is 85 nm. The experimentally obtained resolution σ_{exp} is greater than the ideal resolution due to the aberration caused by the glass plate of the vacuum cell.
- [39] C. Sackett, C. Bradley, M. Welling, and R. Hulet, *Appl. Phys. B* **65**, 433 (1997).
- [40] S. Kadlecek, J. Sebby, R. Newell, and T. G. Walker, *Opt. Lett.* **26**, 137 (2001).
- [41] J. J. Hope and J. D. Close, *Phys. Rev. Lett.* **93**, 180402 (2004).
- [42] Y. Takahashi, K. Honda, N. Tanaka, K. Toyoda, K. Ishikawa, and T. Yabuzaki, *Phys. Rev. A* **60**, 4974

- (1999).
- [43] A. Kuzmich and E. S. Polzik, “Atomic continuous variable processing and light-atoms quantum interface,” in *Quantum Information with Continuous Variables*, edited by S. L. Braunstein and A. K. Pati (Springer Netherlands, Dordrecht, 2003) pp. 231–265.
- [44] V. G. Lucivero, R. Jiménez-Martínez, J. Kong, and M. W. Mitchell, *Phys. Rev. A* **93**, 053802 (2016).
- [45] M. Gajdacz, P. L. Pedersen, T. Mørch, A. J. Hilliard, J. Arlt, and J. F. Sherson, *Rev. Sci. Instrum.* **84**, 083105 (2013).
- [46] M. K. Tey, Z. Chen, S. A. Aljunid, B. Chng, F. Huber, G. Maslennikov, and C. Kurtsiefer, *Nat. Phys.* **4**, 924 (2008).
- [47] E. W. Streed, A. Jechow, B. G. Norton, and D. Kielpinski, *Nat. Commun.* **3**, 933 (2012).